Polylysine-coated surfaces drive competition in chemical reaction networks to enable molecular information processing

A. Hazal Koyuncu,[1,2] Jacopo Movilli,[1] Sevil Sahin,[1] Dmitrii V. Kriukov,[1,2] Jurriaan Huskens,* [1] Albert S. Y. Wong*[1,2]

[1] Department of Molecules and Materials & MESA+ Institute, University of Twente, Drienerlolaan 5, 7522 NB Enschede, The Netherlands

[2] BRAINS (Center for Brain-inspired Nano Systems), University of Twente, Drienerlolaan 5, 7522 NB Enschede, The Netherlands

* E-mail: albert.wong@utwente.nl ; j.huskens@utwente.nl

Keywords: chemical reaction network; systems chemistry; molecular information processing; feedback loops; molecular nanofabrication.

Abstract

This work describes a competing activation network, which is regulated by chemical feedback at the liquid-surface interface. Feedback loops dynamically tune the concentration of chemical components in living systems, thereby controlling regulatory processes in neural, genetic, and metabolic networks. Advances in systems chemistry demonstrate that chemical feedback could be designed based on similar concepts of using activation and inhibition processes. Most efforts, however, are focused on temporal feedback whereas biological networks are maintained by the interplay between temporal and spatial organization. Here, we designed a feedback system which consists of a simple acid-base equilibrium that can be perturbed by two opposing activation processes. Crucially, one of the activation processes is immobilized (or localized) on the surface of a microfluidic channel using poly-L-lysine (PLL). We measured the capacity of the PLL-coated channels to resist changes in pH in flow using a pH-sensitive indicator, phenol red, and showed that this capacity can be increased by employing polyelectrolyte multilayers. Specifically, we found that the rate of local activation (*i.e.*, the deprotonation of the immobilized lysine residues) could be significantly increased to delay the otherwise fast equilibrium. This effect allowed for encoding read and write operations, providing the potential to bestow CRNs with the capacity of molecular information processing.

Introduction

Biology exploits spatial organization to control signal transduction in biochemical networks.[1,2] Ongoing efforts in systems chemistry demonstrate that feedback loops—sets of chemical reactions that represent the smallest possible modules in such networks[3]—may be carefully designed to display behavior ubiquitous in living systems (*e.g.,* bistability, oscillations, and other modes of transient behavior).[4] Many different schemes for interconnected feedback loops exist in theory,[1] and tethering molecular reactions on a surface in particular could provide an attractive strategy to create feedback loops capable of local regulations of (bio)chemical reactions.[5,6] The practical realization, however, requires careful considerations in balancing the reaction rates involved in the activation and inhibition processes.[7]

The design of chemical reaction networks (CRNs) is based on relatively simple network motifs,[8] limited to few possibilities to connect feedback loops.[9] Methods that enable a delay time in (often opposing) feedback loops and maintain out-of-equilibrium conditions are therefore essential in the *de novo* design.[10] On the one hand, previously reported CRNs use synthetic strategies to implement rate dependency (*e.g.*, driven by enzymatic[11–13] or acid-base reactions[14–17]) and concentration dependency (*e.g.*, driven by aggregation,[18,19] or phase separation[20,21]) to create sufficient balance in the delay time. On the other hand, microfluidics[22–24] is employed to maintain reactions in well-mixed open reactors—so-called continuous flow stirred tank reactors (CFSTR)[11,25]. We

question how we can leverage methods in the fabrication of microfluidic systems to balance feedback loops and incorporate the spatial control thereof.

Here, we designed a new method for controlling feedback loops. Fig. 1a depicts the network motif which consists of an equilibrium reaction that can be perturbed by two opposing activation processes, one of which is immobilized on a surface. We used poly-L-lysine (PLL) to functionalize the surface of microfluidic channels as it can bind strongly to glass and polydimethylsiloxane (PDMS),[26] while providing free amine groups as the reactive layer (Fig. 1b). We first demonstrated that control over local activation allows for tuning the strength of the chemical feedback, and developed a mathematical model to support our findings. We then created polyelectrolyte multilayers (PEMs) to change the capacity, and thereby the rate of the deprotonation of the immobilized lysine residues. Finally, we demonstrate that the high control over the stimuli-response curves of PEM surfaces allows for encoding read and write operations.

Results and Discussion

Competing activation as a result of a three-stage process. Our experimental setup consists of low-pressure pumps that continuously feed the PLL-coated channel with an acid, a base, and a pH indicator (phenol red, *I*) (Fig. 2a). We first developed a mathematical model (Supplementary Information S4) to simulate how the competition between the bulk activation and the local activation could occur as part of a three-stage process (Fig. 2b): *i)* an acid (indicated as H^+) is used to protonate, to 'charge', the free amine groups of the lysine residues that are immobilized on the surface. The state of phenol red (protonated form, I_1, or deprotonated form I_2) depends on the pH. In this stage, only phenol red in state I_1 should be present in the channel; *ii)*, a base (indicated as '-') is used to change the pH which forces the transition from I_1 into I_2. The reactive layer, however, causes the opposite transition by either protonating phenol red or neutralizing the base locally; *iii)* the capacity of the reactive surface is effectively limited by the number of lysine residues available in the reactive layer and the system establishes a steady state concentration of I_2, or more specifically, the ratio $[I_2]/[I_1]$.

We then used fluorescein-labelled PLL (Mw=15-30kDa, and 0.03-0.1% fluorescein) to confirm that PLL is indeed immobilized on, and homogeneously distributed across the channel (Supplementary Information, Fig. S6). We set the pumps to change the input pH in the channel in a sequence that alternates between pH 3 and 10, and determined the output of $[I_2]/[I_1]$ using an absorbance detector connected to the outflow of the channel. The output signal follows the pattern of the input pH, and in accordance with the predictions from the model, the output signal is slightly delayed compared to the input pH. The observation that this readout remains consistent throughout multiple cycles demonstrates that our experimental platform can establish a robust readout of the intended competing activation network. To ensure that the coating remained anchored on the surface, we also demonstrated that the fluorescence intensity in the channels is unchanged over the course of the experiment (Supplementary Information, Fig. S6).

Capacity of PLL-coated devices. Like a buffer, the PLL-coated channel has the capacity to resists changes in pH. We determined this capacity by comparing the apparent delay in the output signals of a PLL-coated and an uncoated device (Fig. 3a). An abrupt change in pH is introduced after 15 min, whereafter we determined the time it takes for the output signal to change from 0 to 1 (*i.e.*, the normalized values for a low to a high $[I_2]/[I_1]$). This 'delay time', t_{delay}, represents the time required to recover 50% of the initial system with uncharged lysine residues in the channels (Supplementary Information, S4.3). We measured this value in our experiments by subtracting the delay time of an uncoated device (t^0, wherein the delay of a signal arises from the time required for transport from the device to detector) from the delay in the coated device (t^1): $t_{delay} = t^1 - t^0$.

For instance, the delay time under the conditions depicted in Fig. 3a is 0.8 min. Supplementary Information Fig. S9 shows that the t_{delay} decreases as a function of flow, especially at higher flow rates (k_f > 7.8 µL min^{-1}). This observation suggests that there is a regime wherein the reactive layer can compete with the base but that beyond a specific flow rate, the role of the reactive layer diminishes. This behavior at pH 10 was also observed in our simulations. The simulations showed that the delay could significantly increase at lower pH values (blue lines). This trend, however, could not be observed in our experiments (red symbols). Instead, we observed that t_{delay} did not change significantly as a function of pH.

In order to understand the discrepancy between the experiments and simulations, we performed extended simulations in Supplementary Information S4.4. The phase plots revealed how the concentration of the reactive layer (*i.e.*, the concentration of available amine groups on the surface) could influence the dependencies of the system as a function of flow and pH. Fig. 3b highlights that the delay time is highly dependent on the effective concentration of amine groups, and that the single-layer devices do not show the same dependency. We therefore used layer-by-layer deposition[27] to develop a polyelectrolyte multilayer (PEM)-coated surface (Supplementary Information, S5.3). To our satisfaction, we observed that the t_{delay} in a PEM-coated device (with three layers), indeed, followed the same trend as predicted in the model. Notably, the delay time at pH 8 became much slower, exceeding the time of our experiments (Supplementary Information, Fig. S10). Nevertheless, we observed a significant increase in the delay time when we compared the responses across the examined pH range in the three-layer devices with the single-layer ones.

Influence of poly-electrolyte multilayers on the relative rate of activation. We validated the change of the total mass as a function of the deposition of PEMs, using a technique called quartz crystal microbalance (QCM). Fig. 4a shows that the change in resonance frequency (Δf) increases linearly as a function of the number of polyelectrolyte layers[28,29] (real-time data of QCM are appended to Supplementary Information, Fig. S7). We chose polystyrene sulfonate, PSS, as it can be considered a 'strong' polyanion (pK_a= 2). That is, it ensures a permanent negative charge in the pH range of our experiments (pH=3-10).[30] We observed a smaller Δf value for the first layer (which represents the interaction between SiO_2 and PLL) compared to the Δf-values of subsequent layers (which represent the interactions between PSS and PLL). The Δf value for the first layer can be used to validate that the concentration of available amine groups in a single-layer coating is in agreement with simulations (Supplementary Information, S5.5). We note that Δf values for the subsequent layers in PEMs represent the polyelectrolyte mass as well as the water molecules intercalated between the layers,[27] limiting the possibilities to quantify the number of lysine residues per added layer. Overall, the linear trend shows that the concentration of PLL on the surface can be increased using PEM deposition. The effective concentration of 'free' amine groups, however, may only be increased with one additional layer of PLL (as these charges in subsequent layers are shielded due to the ion-ion interactions with PSS).[29,31]

We compared the devices comprising PEM coatings (3, 5, and 13 layers) with devices with and without a single-layer PLL coating (Fig. 4b). The experiment is similar to the previously described procedure: An abrupt change in pH is introduced after 30 min, whereafter we determined the time it takes for the output signal to change from 0 to 1 at pH 8. This change in pH is then followed by the recharging of the surface, thus recovering the acidic condition (pH 3), and the cycle was repeated 3-5 times (Supplementary Information, S6). We found that the delay time did not change significantly for PEMs with more than three layers. In accordance with the linear trend observed in Fig. 4a, a maximum PLL density on the surfaces is obtained by one additional PLL layer (thus, PEM with three layers: PLL/PSS/PLL). Importantly, Fig. 4b shows that the rate of the competing activation and the charging step in the PEM-coated devices is significantly different compared to a single-layer device.

Control over activation rates enables encoding of molecular information processing. Since the competing activation step is slow, we examined whether the time at which the system is maintained at the basic pH, Δt_B, can be used for encoding information (Fig. 5a). The time at which the system is maintained at the acidic pH, Δt_A, can be used to reset the device. Depending on the choice of the time intervals for the input pH (Δt_A and Δt_B), one can

encode information such as the message 'CRN@UT' (our research group at the University of Twente, Fig. 5b). For this demonstration we used a sequence with Δt_B=5, 20 min and Δt_A=10 min to produce an output pattern comprising multiple local maxima. We then assigned the output as (1) a 'dash', when 0.75 < local maxima < 1.0, or (2) a 'dot', when 0.25 < local maxima < 0.5, to yield the corresponding Morse code for 'CRN@UT'. The runtime of the experiment can be reduced or the density of information can be increased when shorter time intervals for the input pH (Δt_B).

Because the competing activation step is slow, it also provides opportunities to introduce perturbations with Δt_A, allowing for more complex information processing strategies. Fig. 5c depicts three types of outputs wherein we varied the Δt_A (indicated with *i-iii*); *i)* In the absence of perturbations, we observed the same shape with slow activation as observed earlier in Fig 4b and Fig 5b. *ii)* The introduction of a series of perturbations of Δt_A=1 min, essentially, created a complex-valued input. The observation that the pulse signal is transformed into a sinusoidal signal indicates that our device can function as a digital-to-analog signal processor.[32] *iii)* Upon a reduction of the perturbations to Δt_A=0.5 min, we observed that the overall shape of the unperturbed signal is conserved but that local maxima were developed on it. This result demonstrates that the output can be tuned based on the relative timing of the input 'spikes', providing opportunities to explore encoding and decoding schemes used in neuromorphic computing.[33,34] Hence, the reactive surfaces created by PEM-coated microfluidic devices which allows for processing of information, ranging from static to dynamic decoding strategies.

Conclusion

This work showed that respective rates in competing activation processes can be tuned using the poly-L-lysine immobilized on the surface of a microfluidic channel. Challenges encountered in the experimental realization of robust steady-state output in CRNs often relates to finding the balance between the reaction rates of various feedback loops in the network. We explored the potential of using a surface-coupled reaction to create competing activation processes around a very simple acid-base equilibrium. We demonstrated that the obtained output signals are not only tunable and robust, but also applicable for information processing purposes. The incorporation of other functional groups in the reactive layer,[35,36] or the fabrication of devices with a greater control over the surface-to-volume ratio,[37,38] could maximize the potential of PLL-coated surfaces in the design of chemical feedback systems.to extend this approach to many other chemical reactions. We envision that the application of reactive surfaces in microfluidic devices as demonstrated here will enable the design of novel CRNs with feedback loops capable of local regulations of biochemical reactions.

Experimental Methods

Chemicals. Chemicals were obtained commercially and were used without purification. Standard solution of sodium hydroxide (NaOH, 0.1 M) was purchased from Fluka and hydrochloric acid solution (HCl, 32%) was purchased from Merck. Poly-L-lysine hydrobromide (PLL, 15-30 kDa) and poly- L-lysine hydrobromide labelled with fluorescein-5-isothiocyanate (PLL-FITC$_{0.3\text{-}1\%}$, 15-30 kDa) were purchased from Merck. Poly(sodium 4-styrenesufonate sodium salt, 1000 kDa) (PSS) was purchased from Sigma Aldrich. Phenol Red was purchased from Sigma Aldrich. VeroClear-RGD 810 polymer material was purchased from Stratasys for 3D printing. SYLGARD™ 184 silicone elastomer kit was purchased from Dow. Water is purified using a Millipore Milli-Q lab water system. See Supplementary Information S1 further information. This section includes details on equipment, materials and software.

Fabrication of microfluidic channels. The upper layer of the microfluidic channels was fabricated using a two-step process: The devices were designed in Solidworks® and printed (Stratasys Objet Pro 30 3D-Printer) to yield a mal. A mixture of curing agent with silicone elastomer base (1:10 m/m, degassed *in vacuo*) was poured into the mal, and was allowed to polymerize in an oven at 75 °C for 30 minutes. PDMS was bonded with glass slide after activation of the surfaces, for which A ZEPTO plasma oven from Diener Electronic was used. Details on the

fabrication process can be found in Supplementary Information, S2. Note: This section includes validations that the devices (with internal volumes ranging from 9-30 mL) can provide adequate mixing at flow rates between at least 3-10 µL min^{-1}. We chose to use a device with a 9 µL channel because this device provided the highest surface-to-volume ratio among the available set.

Functionalization of channels with PLL and PEM. Microfluidic channels were fabricated using a two-step process described above in *fabrication section*. An oxygen plasma treatment was used to activate the surfaces of the microfluidic devices, after which we rinsed the devices (10x its internal volume) with a solution of PLL in water (0.5 g L^{-1}). After equilibration (5-10 min), excess solution in the channels was thoroughly washed with water (50x its internal volume). Further functionalization were performed using layer-by-layer technique, for which we used CETONI Elements software to automate the above mentioned procedure. PLL and PSS solutions were prepared (0.5 g L^{-1} in water) and transferred into glass syringes and mounted on low-pressure pumps. For details, see Supplementary Information, S5.

Simulations. Simulations were performed using Matlab ®. Trajectories depicted in Fig. 2 and Fig. 3b are simulated using numerical integration. In our model, the rates of concentration changes are based on the consumption, the production, and the continuous in- and outflow of the species in the network. The concentration of phenol red was calculated using the standard Henderson-Hasselbalch equation (log $A^-/HA=pH-pK_a$) between each time-interval of the numerical integration. The model was further used to define the delay time as the time required to recover 50% of the 'initial system' and to examine the influence of pH and flow in the network. For further details, see Supporting Information, S4.

QCM measurements. Quartz crystal microbalance (QCM) experiments were performed using silicon dioxide (SiO_2)-coated quartz sensors. The experiments were performed using dissipation set-up at 22 °C. The sensors were first treated with UV-ozone cleaner for 30 min, and subsequently dipped in 2% sodium dodecyl sulphate solution for 45 minutes at 37 °C, sonicated for 5 minutes. The sensors were rinsed excessively with water, and dried with a gentle flow of nitrogen and treated again with UV-ozone cleaner for 45 min. PLL and PSS solutions were prepared (0.5 g L^{-1} in water). The deposition on the sensor surface started with rinsing sensor surfaces with Milli-Q water, then followed by consecutive cycles of PLL and PSS layers. The real-time change in frequency and dissipation response between 3^{rd} and 9^{th} harmonics were analyzed using Q-Sense. See Supplementary Information Fig. S7 for further information.

Flow experiments. Flow experiments were performed using a flow setup that consists of low-pressure pumps connected to a microfluidic channel. HCl (1 mM), NaOH (1 mM), and phenol red (0.45 mM) were prepared and transferred into glass syringes and mounted on low-pressure pumps. CETONI Elements software was used to program low-pressure pumps in the flow experiments shown in Fig. 3, 4, and 5 (see Supplementary Information S6 for further information on the sequences used in each experiment). The same software was used to analyze the absorbance data (see Supplementary Information S3 for details of the experimental setup).

Acknowledgements

A.S.Y.W. supervised and planned the project. A.S.Y.W., J.H., A.H.K. and J.M. conceived the project. A.H.K. performed the experiments. A.S.Y.W. designed the mathematical model and performed the simulations. S.S. designed and performed the QCM experiments. A.S.Y.W., A.H.K. and D.V.K. designed of the experimental setup. All authors contributed to writing the manuscript. The project is supported by the Netherlands Organization for Scientific Research (NWO, Veni Grant 202.155 to A.S.Y.W; TOP grant 715.015.001 to J.H.) and by the Weijerhorst Foundation.

References

1. B. N. Kholodenko, *Nat. Rev. Mol. Cell Biol.* **2006**, *7*, 165–176.

2. M.C Good, J. G. Zalatan, W. A. Lim, *Science,* **2011***, 332*, 680–686.

3. J. J. Tyson, K. C. Chen, & B. Novak, *Curr. Opin. Cell Biol.* **2003**, *15*, 221–231.

4. J. H. van Esch, R. Klajn,& S. Otto, *Chem. Soc. Rev.* **2017**, *46*, 5474–5475.

5. G. Menon, J. Krishnan, *Nat. Commun.* **2021**, *12*, 5357.

6. S. Clamons, L. Qian, E. Winfree, *J. R. Soc. Interface* **2020**, *17*, 20190790.

7. B. A. Grzybowski, W. T. S Huck, *Nat. Nanotechnol.* **2016**, *11*, 585–592.

8. A. S.Y. Wong, W. T. S. Huck, *Beilstein J. Org. Chem.* **2017**, *13*, 1486–1497.

9. G. Ashkenasy, T. M. Hermans, S. Otto, A. F. Taylor, *Chem. Soc. Rev.* **2017***, 46*, 2543–2554.

10. B. Novák, J. J. Tyson, *Nat. Rev. Mol. Cell Biol.* **2008**, *9*, 981–991.

11. S. N. Semenov, A.S.Y. Wong, R. M. van der Made, S.G.J. Postma, J. Groen, H.W.H van Roekel, T.F.A de Greef, W.T.S Huck, *Nat. Chem.* **2015***, 7*, 160–165.

12. C. G. Pappas, I. R. Sasselli, R. V. Ulijn, *Angew. Chem.* **2015**, *127*, 8237–8241.

13. A. A. Pogodaev, C. L. F. Regueiro, M. Jakštaitė, M. J. Hollander, W. T. S. Huck, *Angew. Chem.* **2019**, *58*, 14539–14543.

14. G. Hu, J. A. Pojman, S. K. Scott, M. M. Wrobel, A. F. Taylor, *J. Phys. Chem. B*. **2010**, *114*, 14059–14063.

15. J. J. Armao, J.-M. Lehn, *J. Am. Chem. Soc.* **2016**, *138*, 16809–16814.

16. X. Fan, A. Walther, *Angew. Chem.* **2021**, *133*, 3663–3668.

17. K. Kovacs, R. E. McIlwaine, S. K. Scott, A.F. Taylor, *J. Phys. Chem.* **2007**, *111*, 549–551.

18. J. M. A. Carnall, C.A. Waudby, A. M. Belenguer, M.C.A Stuart, J. J-P. Peyralans, S. Otto, *Science* **2010**, *327*, 1502–1506.

19. S. Maiti, I. Fortunati, C. Ferrante, P. Scrimin, L. J. Prins, *Nat. Chem.* **2016**, *8*, 725–731.

20. M. G. Howlett, A. H. J. Engwerda, R. J. H. Scanes, S. P. Fletcher, *Nat. Chem*. **2022**, *14*, 805–810.

21. J. Boekhoven, W. E. Hendriksen, G. J. M. Koper, R. Eelkema, J.H. van Esch, *Science* **2015**, *349*, 1075–1079.

22. B. T. Ginn, B. Steinbock, M. Kahveci, O. Steinbock, *J. Phys. Chem.* **2004**, *108*, 1325–1332.

23. C. J. Kastrup, M. K. Runyon, F. Shen, R.F. Ismagilov, *Proc. Natl. Acad. Sci. U.S.A.* **2006**, *103*, 15747–15752.

24. A. J. DeMello, *Nature* **2006**, *442*, 394–402.

25. I. R. Epstein, K. Showalter, *J. Phys. Chem.* **1996**, *100*, 13132–13147.

26. J. Movilli, A. Rozzi, R. Ricciardi, R. Corradini, J. Huskens, *Bioconjugate Chem.* **2018**, *29*, 4110–4118.

27. I. Reviakine, D. Johannsmann, R. P. Richter, *Anal. Chem.* **2011**, *83*, 8838–8848.

28. X. Zan, B. Peng, D. A. Hoagland, Z. Su, *Polym. Chem.* **2011**, *2*, 2581–2589.

29. K. Tang, N. A. M. Besseling, *Soft Matter*, **2015**, *12,* 1032–1040.

30. E. N. Durmaz, S. Sahin, E. Virga, S. de Beer, L. C. P. M. de Smet, W.M. de Vos, *Acs. Appl. Polym. Mater.* **2021**, *3*, 4347–4374.

31. D. Kosior, M. Morga, P. Maroni, M. Cieśla, Z. Adamczyk, *J. Phys. Chem. C* **2020**, *124*, 4571–4581.

32. D. Bi, Y. Deng, *IEEE Commun. Mag.* **2021**, *59*, 26–32.

33. Y. van de Burgt, A. Melianas, S. T. Keene, G. Malliaras, A. Salleo, *Nat. Electron* **2018**, *1*, 386–397.

34. Y. Wang, Q. Zhang, H. P. A. G Astier, C. Nickle, S. Soni, F. A. Alami, A. Borrini, Z. Zhang, C. Honnigfort, B. Braunschweig, A. Leoncini, D-C. Qi, Y. Han, E. D. Barco, D. Thompson, C. A. Nijhuis, *Nat. Mater.* **2022**, *21*, 1403–1411.

35. G. Liu, M. Hirtz, H. Fuchs, Z. ZhengLiu, *Small* **2019**, *15*, 1900564.

36. E. Karzbrun, A. M. Tayar, V. Noireaux, R. H. Bar-Ziv, *Science* **2014**, *345*, 829–832.

37. A. J. Genot, A. Baccouche, R. Sieskind, N. Aubert-Kato, N. Bredeche, J. F. Bartolo, V. Taly, T. Fujii, Y. Rondelez, *Nat. Chem.* **2016**, *8*, 760–767.

38. H. Niederholtmeyer, V. Stepanova, S. J. Maerkl, *Proc. Natl. Acad. Sci. U.S.A.* **2013***, 110*, 15985–15990.

Figures.

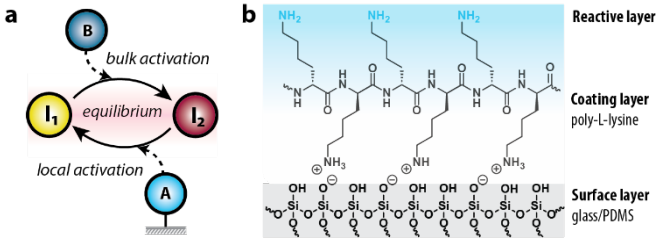

Fig. 1. Competing activation network. a) Network motif wherein two opposing activation processes center around an equilibrium reaction. I_1 and I_2 indicate two possible states of an equilibrium reaction. B indicates a species that can activate I_1, and A indicates a species immobilized on a surface that can activate I_2. b) Reactive surfaces are prepared by adhering poly-L-lysine in microfluidic channels, which surfaces are made from glass or PDMS (see Supplementary Information S2).

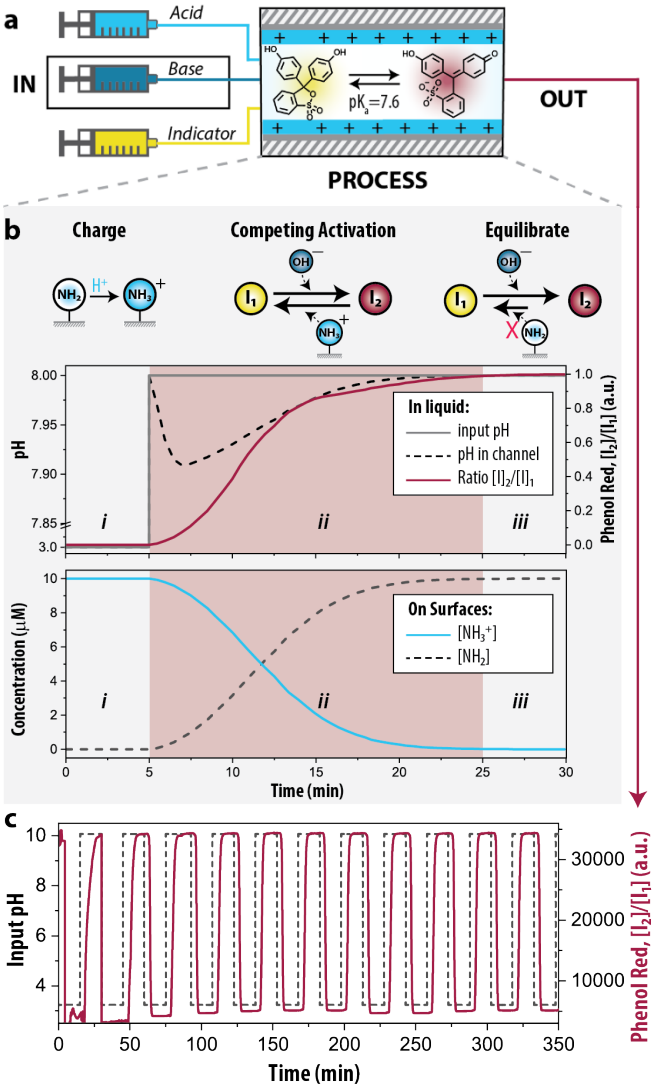

Fig. 2. Experimental Setup. (a) Schematic representation of the flow setup with the input pH controlled by syringes mounted on low-pressure pumps and the output signal detected in the outflow (see details in Supplementary Information Fig. S2). (b) Simulated time series showing the three-stage process depicted as (*i*) charge, (*ii*) competing activation, and (*iii*) equilibrate. The model consists of a set of five differential equations (see details in Supplementary Information S4). (c) Experimental time series showing that the network can produce two different states of phenol red. The input pH (grey line) is maintained for 15 min at alternating pH values, 3 and 10. The output signal (red line) is determined by integrating the absorbance at 550-570 nm. The units of the signal are arbitrary; below pH 6.8 the signal is considered low. Above pH 8.2, phenol red turns in a pink color and hence the sharp increase to a high signal (*i.e.*, a high $[I_2]/[I_1]$ ratio). Initial conditions for (b) and (c): $[I]_0$ = 22.5 μM. flow rate = 3.33 μL min^{-1}.

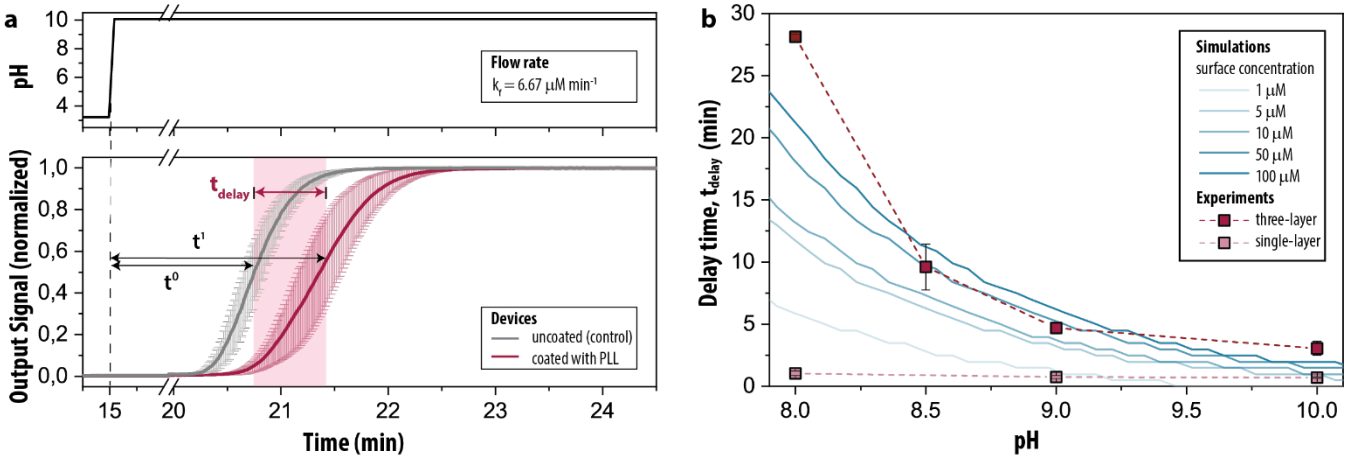

Fig. 3. Observed delay time. a) Time series of the input pH, and the output signal of uncoated (grey line), and PLL-coated devices (red line). Error margins are based on a triplicate experiment. Unity-based normalization is applied to create an output with "0" and "1" representing the minimum and maximum output value, respectively. Initial conditions: $[I]_0$ = 22.5 µM. The determination of the values for delay time depicted in the graph. b) Delay time as a function of pH at k_f = 6.67 µL min^{-1}. Data points show the experimentally determined time delay in a single- and three-layered devices (details are appended to Supplementary Information S6.3-S6.4), and blue lines show the simulated time delay at various surface concentrations. Error bars depict the standard deviations of triplicate experiments.

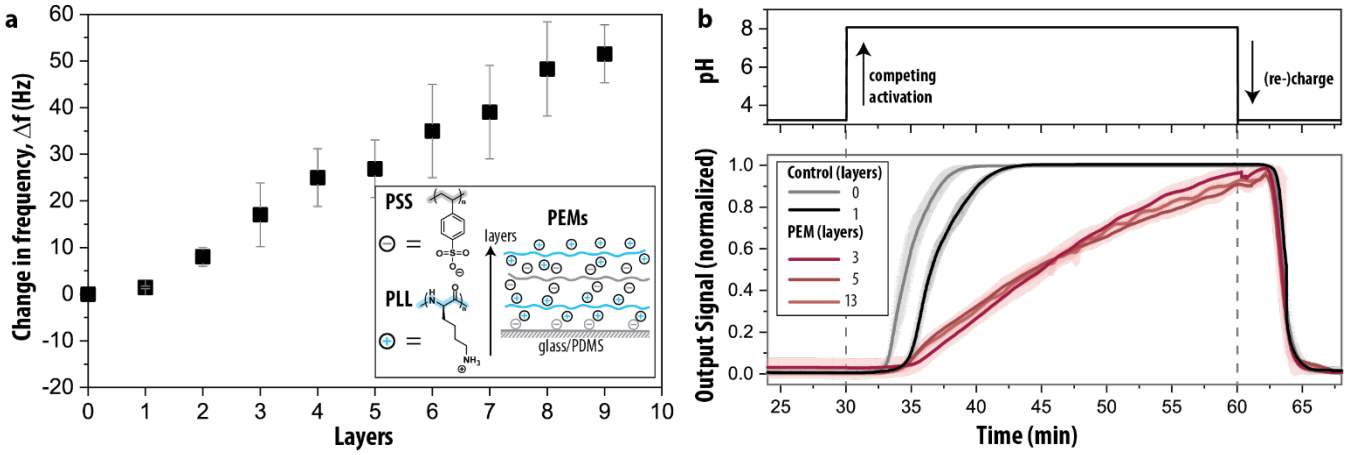

Fig. 4. Polyelectrolyte multilayers expand the capacity of local activation. a) The method of developing a coating with alternating polyelectrolyte layers was confirmed using quartz crystal microbalance (QCM) and the 5th overtone is displayed for change in the frequency, Δf. Error bars depict the standard deviation based on triplicate measurements with different sensors. The polycation (poly-L-lysine, PLL) and the polyanion (polystyrene sulfonate, PSS) are depicted here as a single layer for simplicity. b) Experimental time series of the input pH, and the output signal of PEM-coated devices. Error margins depict the standard deviation. Initial conditions: $[I]_0$ = 22.5 µM, flow rate= 6.67 µL min^{-1}. Devices with PEM coating were prepared using layer-by-layer deposition (see Methods).

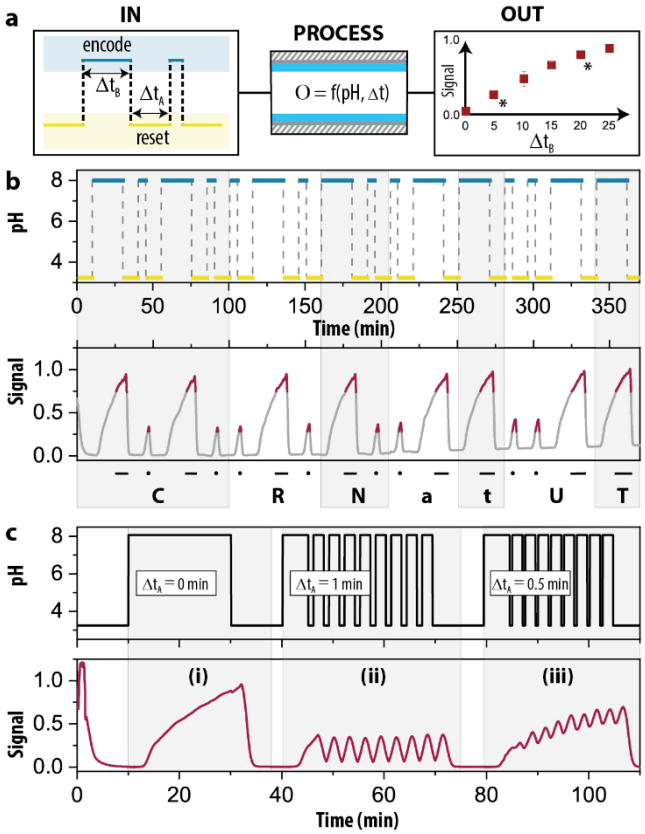

Fig. 5. Molecular information processing with a competing activation network. a) Schematic representation of the encoding strategy, wherein the time-interval in the pH input (Δt_A and Δt_B) is converted into a signal of defined height. Asterisk depicts the conditions used for experiment in panel (b). Demonstration of b) encoding and decoding a Morse code, and c) signal transformation, by comparing the response i) under unperturbed conditions, and under perturbed conditions wherein ii) Δt_A=1 min, iii) Δt_A=0.5 min. Initial conditions for (b) and (c): $[I]_0$ = 22.5 µM, flow rate = 6.67 µL min^{-1}.